Type Ia Supernovae Yielding Distances with 3-4% Precision

Patrick L. Kelly[1][*], Alexei V. Filippenko[1], David L. Burke[2],
Malcolm Hicken[3], Mohan Ganeshalingam[4], Weikang Zheng[1]

Department of Astronomy, University of California, Berkeley, CA 94720-3411, USA

SLAC National Accelerator Laboratory, 2575 Sand Hill Rd, Menlo Park, CA 94025

Harvard-Smithsonian Center for Astrophysics, Cambridge, MA 02138, USA

Lawrence Berkeley National Laboratory, 1 Cyclotron Road, Berkeley CA 94720

[*]To whom correspondence should be addressed; E-mail: pkelly@astro.berkeley.edu.

The luminosities of Type Ia supernovae (SN), the thermonuclear explosions of white dwarf stars, vary systematically with their intrinsic color and light-curve decline rate. These relationships have been used to calibrate their luminosities to within ~ 0.14–0.20 mag from broadband optical light curves, yielding individual distances accurate to ~ 7–10%. Here we identify a subset of SN Ia that erupt in environments having high ultraviolet surface brightness and star-formation surface density. When we apply a steep model extinction law, these SN can be calibrated to within ~ 0.065–0.075 mag, corresponding to ~ 3–4% in distance — the best yet with SN Ia by a substantial margin. The small scatter suggests that variations in only one or two progenitor properties account for their light-curve-width/color/luminosity relation.

The disruption of a white dwarf by a runaway thermonuclear reaction can create a SN explosion luminous enough to be visible across the last ~ 10 Gyr of the cosmic expansion. The successive discoveries that intrinsically brighter SN Ia have light curves that fade more slowly (*1*) and have bluer color (*2*) made it possible to determine the luminosity (intrinsic brightness) of individual SN Ia with ~ 0.14–0.20 mag accuracy, using only the SN color and the shape of the optical light curve. Through comparison between the intrinsic and apparent brightness of each SN Ia, a distance to each explosion can be estimated. Employing the precision afforded by light-curve calibration, measurements of luminosity distances to redshift $z \lesssim 0.8$ SN Ia showed that the cosmic expansion is accelerating (*3*, *4*).

Currently available constraints on the cosmic expansion history do not identify the physical cause of the acceleration. While wide-field surveys are expected to discover large numbers of SN Ia during the next decade, a $\sim 10\%$ average difference exists between the calibrated luminosities of SN Ia in low-mass and high-mass host galaxies (*5–8*), and the colors of SN Ia (*9, 10*) show a dependence on photospheric velocity.

Sufficiently precise calibration of SN Ia would considerably reduce the importance of these systematic effects for cosmological measurements, so recent efforts have sought to improve calibration accuracy by examining features of SN Ia spectra (*9–12*), infrared luminosity (*13, 14*), and their host-galaxy environments (*5–7, 15*). A Supernova Factory analysis found that SN Ia having greater Hα emission within $\sim 1\,\mathrm{kpc}$ of the explosion site (uncorrected for extinction) were, on average, $\sim 0.1\,\mathrm{mag}$ less luminous, after light-curve correction (*15*). Flexible models for light curves, including principal component analysis, have also recently been applied to synthetic photometry of SN spectral series, and show useful improvement (*16*). While these methods may yield calibration to within ~ 0.10–$0.12\,\mathrm{mag}$ ($\sim$ 5-6% in distance), they require measurements significantly more costly to acquire than broadband optical imaging.

Here we show that SN Ia identified from only photometry of a circular $r = 5\,\mathrm{kpc}$ aperture at the SN position can be used to measure individual distances with $\sim$ 3–4% accuracy. Our sample consists of $0.02 < z < 0.09$ SN Ia in the Hubble flow, and is assembled from the collections of published Lick Observatory Supernova Search (LOSS) (*17, 18*), Harvard-Smithsonian Center for Astrophysics (CfA), and Carnegie Supernova Project (CSP) light curves described in Table S1. Table S2 shows how we construct our light-curve sample.

We compute distance moduli using the MLCS2k2 light-curve fitting algorithm (*19*) available as part of the SuperNova ANAlysis (SNANA; v10.35) (*20*) package. MLCS2k2 parameterizes light curves using a decline parameter Δ and an extinction to the explosion A_V, and solves simultaneously for both. Model light curves with higher values of Δ fade more quickly and are intrinsically redder.

To model extinction by dust, MLCS2k2 applies the O'Donnell (*21*) law, parameterized by the ratio between the V-band extinction A_V and the selective extinction $E(B-V) = A_B - A_V$. While $R_V = A_V/E(B-V)$ has a typical value of ~ 3.1 along Milky Way sight lines (*22*), lower values of R_V yield the smallest Hubble-residual scatter for nearby SN Ia (*23*). A Hubble residual (HR $\equiv \mu_{\mathrm{SN}} - \mu_z$) is defined here as the difference between the distance modulus to the SN inferred from the light curve, μ_{SN}, and that expected for the best-fitting cosmology, μ_z. We find that $R_V = 1.8$ minimizes the scatter of Hubble residuals of the SN in our full $0.02 < z < 0.09$ sample, after fitting light curves with values of $1 \leq R_V \leq 4$ in increments of $\Delta R_V = 0.1\,\mathrm{mag}$.

Using images taken by the *GALEX* satellite, we measure the host galaxy far- and near-ultraviolet (FUV and NUV, respectively) surface brightnesses inside of a circular $r = 5\,\mathrm{kpc}$ aperture centered on the SN position. We show, in Figure 1, that SN Ia whose apertures have high NUV surface brightness exhibit an exceptionally small scatter among their Hubble

residuals. Among the Hubble residuals of the $N = 17$ SN Ia in environments brighter than $24.5\,\mathrm{mag\,arcsec}^{-2}$, the root-mean-square scatter is $0.073\pm0.010\,\mathrm{mag}$. When we examine only the $N = 10$ SN Ia with distance modulus statistical uncertainty $\sigma_{\mu_{\mathrm{SN}}} < 0.075\,\mathrm{mag}$, the root-mean-square scatter is $0.065\pm0.014\,\mathrm{mag}$. SN 2007bz, which exploded in a high surface-brightness region and has a very large Hubble residual ($0.60 \pm 0.07\,\mathrm{mag}$), is the only SN we exclude when we compute the sample standard deviation. While our $R_V = 1.8$ MLCS2k2 fit to the light curve of SN 2007bz yields $A_V = 0.26 \pm 0.07$ mag, a published BAYESN fit instead favors a higher extinction of $A_V = 0.81 \pm 0.12$ mag (*14*), which would correspond to a significantly reduced Hubble residual. Figure 3 shows the redshift-distance relation for the SN Ia found in environments with high-NUV surface brightness juxtaposed with that for the SN Ia in the entire sample.

To determine the statistical significance of finding N objects with Hubble-residual scatter σ_{HR}, we perform Monte Carlo simulations where we repeatedly randomly select N objects from the parent SN sample after removing $> 0.3\,\mathrm{mag}$ outliers, and calculate the percentage of these random samples with a standard deviation smaller than σ_{HR}. As shown in Table 1, only 0.1% of randomly selected $N = 17$ samples have scatter smaller than the $0.073\pm0.010\,\mathrm{mag}$ we measure for SN Ia in host environments with high UV surface brightness. Distance moduli are expected to include a $\sigma \approx 0.045\,\mathrm{mag}$ random contribution from the peculiar velocities of the host galaxies, given an uncertainty of $300\,\mathrm{km\,s}^{-1}$ and the median $z = 0.027$ sample redshift.

We also estimate the average star-formation surface density ($M_\odot\,\mathrm{yr}^{-1}\,\mathrm{kpc}^{-2}$) within each circular $r = 5\,\mathrm{kpc}$ aperture, when both optical (*ugriz* or *BVRI*) as well as FUV and NUV imaging of the host galaxy are available. While fewer host galaxies have the necessary imaging, Figure 2 shows that the SN having high star-formation density environments also have comparably small scatter in their Hubble residuals. The $N = 11$ SN Ia with apertures having average star-formation surface density greater than $-2.1\,\mathrm{dex}$ exhibit $\sigma_{\mathrm{HR}} = 0.075\pm0.012\,\mathrm{mag}$. Among randomly selected samples, 0.9% have a smaller standard deviation among their Hubble residuals.

The $10\,\mathrm{kpc}$ diameter of the host-galaxy aperture subtends an angle of $1.6''$ at $z = 0.5$ and $1.3''$ at $z = 1$. Therefore, the NUV surface brightnesses of high-redshift SN Ia hosts within a circular $r = 5\,\mathrm{kpc}$ aperture can be measured from the ground in conditions with subarcsecond seeing, making possible high-precision measurements of distances to high redshift.

Given the high UV surface brightness and star-formation density, as well as the star formation evident from Sloan Digital Sky Survey (SDSS) images, the white dwarf progenitors must have relatively young ages. The SDSS composite images in Figure S6 show that the $r = 5\,\mathrm{kpc}$ apertures include stellar populations of multiple ages, and the younger stellar populations are expected to dominate the measured NUV flux. While O-type and early B-type stars having $M \gtrsim 15\,\mathrm{M}_\odot$ are required to produce the ionizing radiation responsible for H II regions, stars with $M \gtrsim 5\,\mathrm{M}_\odot$ with lifetimes of $\lesssim 100\,\mathrm{Myr}$ are responsible for the UV luminosity (*24*, *25*). A delay time of $480\,\mathrm{Gyr}$ would be required

for a SN Ia progenitor to travel $\sim 5\,\mathrm{kpc}$ with a natal velocity of $10\,\mathrm{km\,s^{-1}}$.

The total mass, metallicity, central density, and carbon-to-oxygen ratio of the white dwarf, as well as the properties of the binary companion, likely vary within the progenitor population of SN Ia. In theoretical simulations of both single-degenerate (*26–28*) and double-degenerate (*29, 30*) explosions, the variation of many of these parameters can yield a correlation between light-curve decline rate and luminosity, but the normalization and slope of these predicted correlations generally show significant differences. Therefore, it is likely that variations in only one or two progenitor properties contribute significantly to the light-curve-width/color/luminosity relation of the highly standardizable SN Ia population we have discovered. The asymmetry of the explosion, thought to increase random scatter around the light-curve-width/color/luminosity relation, may be small within this population and may possibly indicate that most burning occurs during the detonation phase (*27*). A reasonable possibility is that the relatively young ages of the progenitor population correspond to a population having smaller dispersion in their ages, leading to more uniform calibration.

As we show in Table 1, for both the full sample and the SN found in UV-bright environments, MLCS2k2 distances computed with $R_V = 1.8$ yield a smaller Hubble-residual scatter than those computed with $R_V = 3.1$. For a handful of well-sampled SN Ia where the extinction is large ($E(B - V) \gtrsim 0.4\,\mathrm{mag}$), the small intrinsic continuum polarization ($\lesssim 0.3\%$) of SN Ia (*31*) allows constraints on the wavelength-dependent polarization introduced by intervening dust (*32*). Analyses of SN 1986G, SN 2006X, SN 2008fp, and SN 2014J find evidence for low values of R_V and blue polarization peaks, consistent with a small grain size distribution (*32*). In these cases, the polarization vector is aligned with the apparent local spiral arm structure, suggesting that the dust is interstellar rather than circumstellar.

A possibility is that SN environments having intense star formation may generate outflowing winds that entrain small dust grains, which might explain the evidence for low R_V and the continuum polarization. Dust particles in the SN-driven superwind emerging from the nearby starburst galaxy M82 scatter light that originates in the star-forming disk, and the spectral energy distribution of the scattered light is consistent with a comparatively small grain size distribution (*33*).

References

1. M. M. Phillips, *ApJ* **413**, L105–L108 (1993).

2. A. G. Riess, W. H. Press, R. P. Kirshner, *ApJ* **473**, 88 (1996).

3. A. G. Riess *et al.*, *AJ* **116**, 1009–1038 (1998).

4. S. Perlmutter *et al.*, *ApJ* **517**, 565–586 (1999).

5. P. L. Kelly, M. Hicken, D. L. Burke, K. S. Mandel, R. P. Kirshner, *ApJ* **715**, 743–756 (2010).

6. M. Sullivan *et al.*, *MNRAS* **406**, 782–802 (2010).

7. H. Lampeitl *et al.*, *ApJ* **722**, 566–576 (2010).

8. M. Childress *et al.*, *ApJ* **770**, 108 (2013).

9. X. Wang *et al.*, *ApJ* **699**, L139–L143 (2009).

10. R. J. Foley, D. Kasen, *ApJ* **729**, 55 (2011).

11. S. Bailey *et al.*, *A&A* **500**, L17–L20 (2009).

12. J. M. Silverman, M. Ganeshalingam, W. Li, A. V. Filippenko, *MNRAS* **425**, 1889–1916 (2012).

13. W. M. Wood-Vasey *et al.*, *ApJ* **689**, 377–390 (2008).

14. K. S. Mandel, G. Narayan, R. P. Kirshner, *ApJ* **731**, 120 (2011).

15. M. Rigault *et al.*, *A&A* **560**, A66 (2013).

16. A. G. Kim *et al.*, *ApJ* **766**, 84 (2013).

17. J. Leaman, W. Li, R. Chornock, A. V. Filippenko, *MNRAS* **412**, 1419–1440 (2011).

18. W. Li *et al.*, *MNRAS* **412**, 1441–1472 (2011).

19. S. Jha, A. G. Riess, R. P. Kirshner, *ApJ* **659**, 122–148 (2007).

20. R. Kessler *et al.*, *PASP* **121**, 1028–1035 (2009).

21. J. E. O'Donnell, *ApJ* **422**, 158–163 (1994).

22. E. L. Fitzpatrick, D. Massa, *ApJ* **663**, 320–341 (2007).

Criterion	σ_{HR} ($R_V = 1.8$)	σ_{HR} ($R_V = 3.1$)
UV and $\sigma_{\mu_{\mathrm{SN}}} < 0.075$	0.128±0.011 (N=50)	0.132±0.011 (N=46)
NUV SB < 24.5	0.065±0.014 (N=10; p=1.0%)	0.107±0.022 (N=8; p=28%)
NUV SB < 24.75	0.070±0.011 (N=12; p=0.7%)	0.100±0.016 (N=14; p=8.0%)
Full UV Sample	0.130±0.009 (N=77)	0.140±0.008 (N=78)
NUV SB < 24.5	0.073±0.010 (N=17; p=0.1%)	0.096±0.011 (N=17; p=1.3%)
NUV SB < 24.75	0.081±0.009 (N=21; p=0.1%)	0.095±0.010 (N=25; p=0.1%)
Full SFR Sample	0.133±0.009 (N=61)	0.141±0.009 (N=62)
$\Sigma_{\mathrm{SFR}} > -2.1$	0.075±0.012 (N=11; p=0.9%)	0.088±0.016 (N=11; p=2.3%)
$\Sigma_{\mathrm{SFR}} > -2.25$	0.094±0.012 (N=18; p=1.2%)	0.110±0.014 (N=18; p=4.5%)

Table 1: The scatter among the Hubble residuals of the highly standardizable SN Ia using $R_V = 1.8$ and $R_V = 3.1$. We compute the standard deviation uncertainty through bootstrap resampling, after >0.3 mag Hubble-residual outliers are removed.

23. M. Hicken *et al.*, *ApJ* **700**, 1097–1140 (2009).

24. S. G. Stewart *et al.*, *ApJ* **529**, 201–218 (2000).

25. S. M. Gogarten *et al.*, *ApJ* **691**, 115–130 (2009).

26. S. E. Woosley, D. Kasen, S. Blinnikov, E. Sorokina, *ApJ* **662**, 487–503 (2007).

27. D. Kasen, F. K. Röpke, S. E. Woosley, *Nature* **460**, 869–872 (2009).

28. S. A. Sim *et al.*, *MNRAS* **436**, 333–347 (2013).

29. D. Kushnir, B. Katz, S. Dong, E. Livne, R. Fernández, *ApJ* **778**, L37 (2013).

30. R. Moll, C. Raskin, D. Kasen, S. E. Woosley, *ApJ* **785**, 105 (2014).

31. L. Wang, J. C. Wheeler, *ARA&A* **46**, 433–474 (2008).

32. F. Patat *et al.*, *ArXiv e-prints*, arXiv:1407.0136 (2014).

33. S. Hutton *et al.*, *MNRAS* **440**, 150–160 (2014).
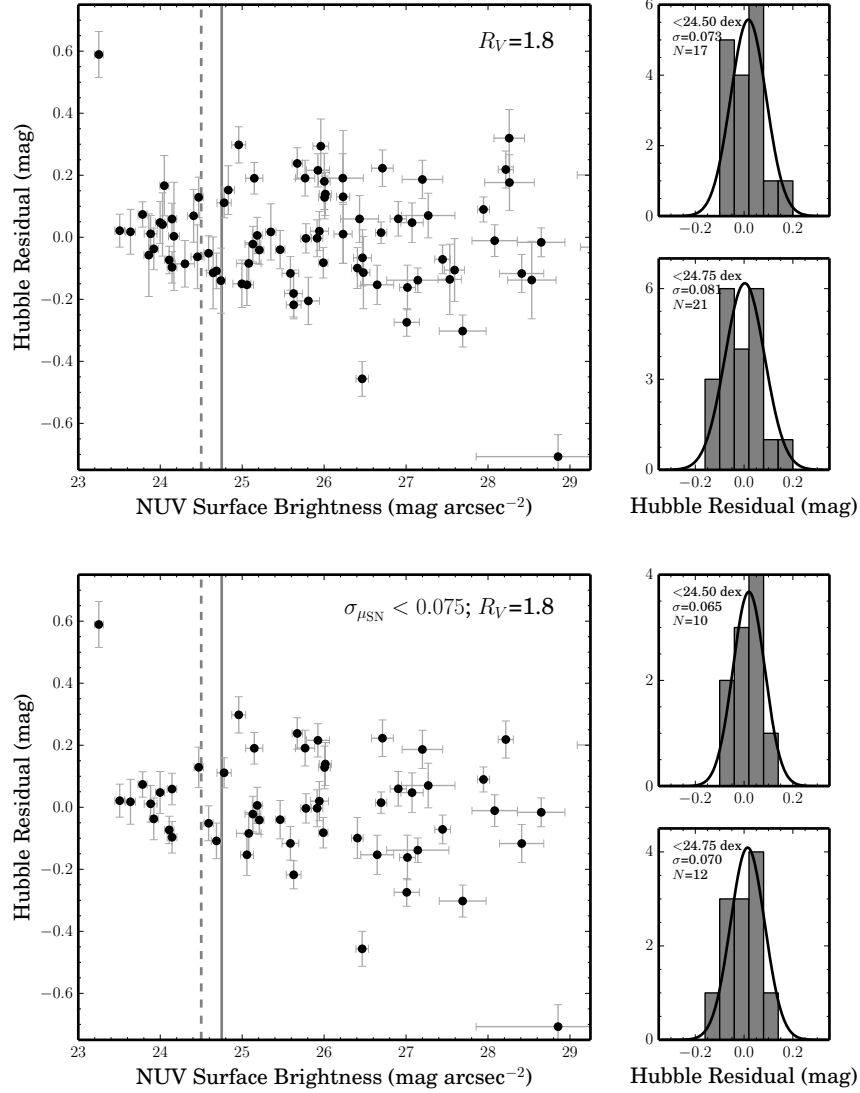
Fig. 1: Hubble residuals against *GALEX* near-UV host-galaxy surface brightness measured inside of a circular $r = 5\,\mathrm{kpc}$ aperture centered on the SN position. Top panels show all SN in sample, while bottom panels include only SN with small statistical uncertainty ($\sigma_{\mu_{\mathrm{SN}}} < 0.075$ mag) in distance modulus. Panels on right show the distributions of Hubble residuals for SN in regions brighter than the $24.75\,\mathrm{mag\,arcsec^{-2}}$ marked by vertical lines in each figure. Dashed vertical lines show more restrictive $24.5\,\mathrm{mag\,arcsec^{-2}}$.
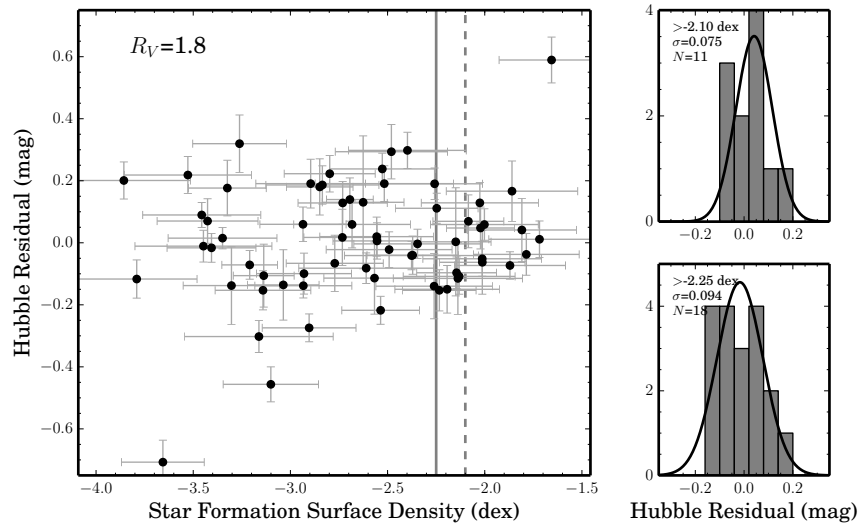
Fig. 2: Hubble residuals against star-formation surface density measured inside of a circular $r = 5\,\mathrm{kpc}$ aperture centered on the SN position. Panels on right show the distributions of Hubble residuals for SN in regions with higher star-formation surface density than the $-2.25\,\mathrm{dex}$ limit marked by a vertical line, and than -2.1, marked by the dashed line, respectively. As shown in Table S2, a smaller number of host galaxies have the optical broadband photometry necessary to estimate the star-formation surface density within the $r = 5\,\mathrm{kpc}$ circular aperture.
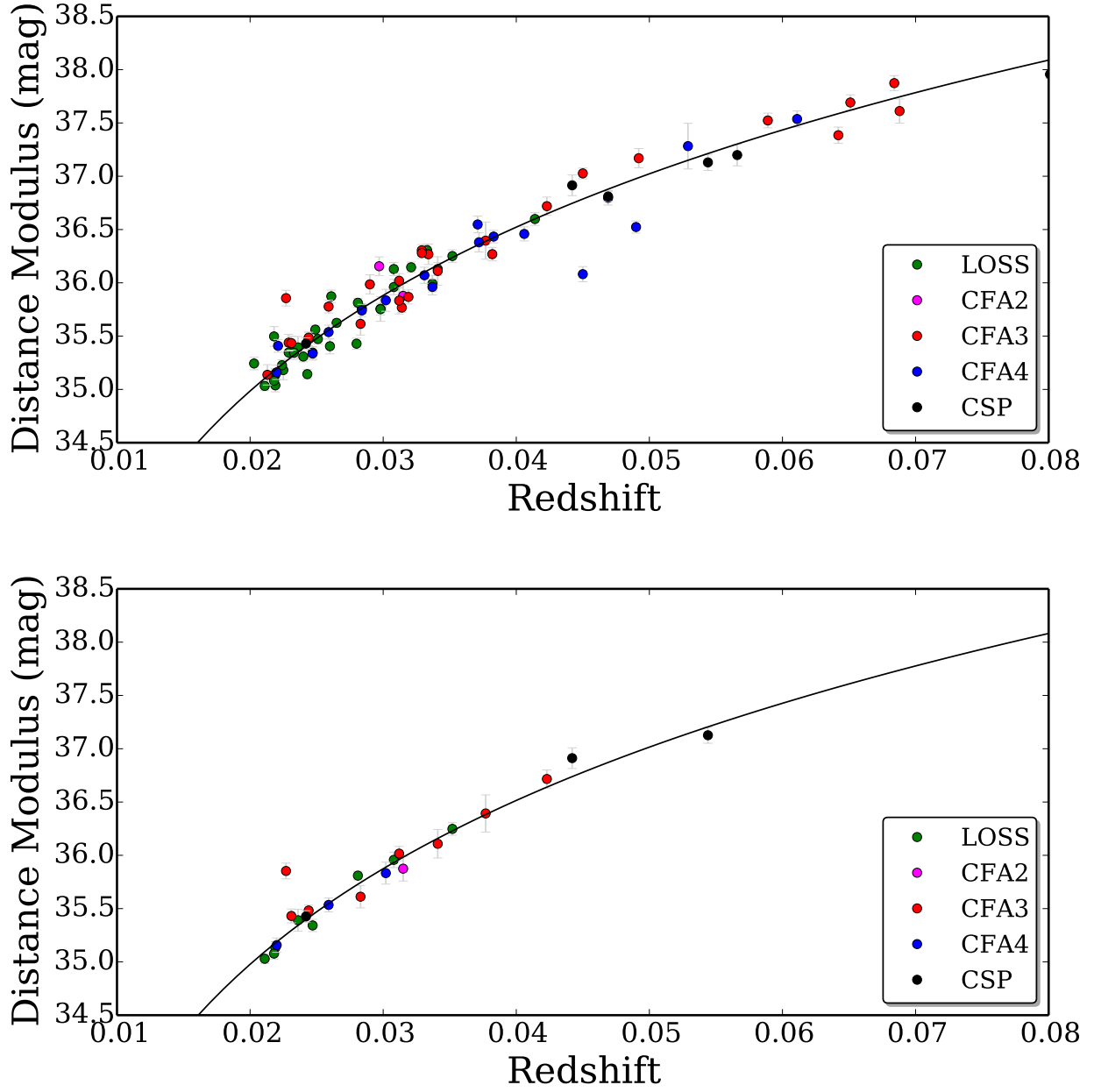
Fig. 3: The SN Ia Hubble redshift-distance relations. Upper panel plots distance modulus μ versus redshift z for SN Ia. Lower panel shows the same relation for SN where the aperture NUV surface brightnesses is brighter than $24.75\,\mathrm{mag\,arcsec^{-2}}$. The color of each point shows the source of the SN light curve. In the lower panel, SN 2007bz is the single object with an outlying distance modulus ($0.60 \pm 0.07\,\mathrm{mag}$).

9

Supporting Online Material

Selection of Light Curves. To include a SN in our sample, we require a photometric measurement before 5 days after *B*-band maximum, at least one photometric measurement after *B*-band maximum, and at least three separate epochs having a signal-to-noise ratio (S/N) > 5 measurement. Only photometry through 50 days after *B*-band maximum enters the fitting with MLCS2k2.

A fraction of the SN in our sample were followed by multiple teams and published in more than one of the light-curve collections listed in Table S1. We selected the light curve according to the order in Table S1, with light-curve collections at the beginning of the list having precedence. Rearranging the order does not significantly change the Hubble-residual statistics that we measure.

In Figure S1, we compare the distance moduli inferred by MLCS2k2 to SN that have a light curve published both by LOSS and in a second collection of light curves. The distances are not affected by the peculiar motions of galaxies, so we include $z < 0.02$ SN that are not part of the Hubble-residual sample. The plot suggests greater agreement between MLCS2k2 $R_V = 1.8$ distance moduli for the SN Ia that explode in regions with high NUV surface brightness, including the several objects too nearby to be in the Hubble-residual sample.

MLCS2k2 Light-Curve Fitting. Except for CSP SN Ia photometry, for which we use magnitudes in the natural system, all fitting is performed to fluxes in the Landolt standard system (*34*). Heliocentric SN Ia redshifts are transformed to the cosmic microwave background (CMB) rest frame using the dipole velocity (*35*). Since MLCS2k2 performs light-curve fitting to rest-frame fluxes, the observed SN fluxes are transformed, prior to fitting, from the observer frame into the rest frame using a K-correction (*36*).

Figures S2 and S3 show the light-curve parameter cuts that we apply to the sample of SN Ia light curves.

Calculating Statistical Significance. Through Monte Carlo simulations, we have assessed the probability that the small Hubble-residual scatter we measure for SN Ia in UV-bright host-galaxy apertures is only a random effect. An additional possibility is that, from random effects, the SN erupting instead in UV-faint regions could have exhibited small apparent Hubble-residual scatter. If we expect that we would have reported this alternative pattern as a discovery, then the *p*-values we compute should be adjusted to account for multiple searches. For n separate searches, the probability of finding at least one random pattern having significance p is $p' = 1 - (1 - p)^n$. We have calculated, assuming a single search, a *p*-value of 0.1% for the measured Hubble-residual scatter of 0.073 ± 0.010 mag for SN Ia in regions with high NUV surface brightness (see Table 1). Assuming instead $n = 4$ separate searches, for example, would yield an adjusted *p*-value of 0.4%.

However, a principal focus of our analysis from its inception was to identify SN Ia in UV-bright, star-forming environments using *GALEX* imaging, motivated by a recent analysis of Hα flux near explosion sites (*15*). Indeed, while high UV surface brightness within the $r = 5\,\mathrm{kpc}$ aperture provides strong evidence for a young stellar population, interpretation of low average UV surface brightness is less straightforward. As shown in Figure S6, the apertures with lower NUV surface brightness consist of a heterogeneous mix of SN in low-mass galaxies having small physical sizes, SN with large host offsets, and SN erupting in old stellar populations. Given the mixed set of environments, it probably would have been unlikely that we would feel we had found a robust pattern. If SN with very small scatter exploded from the oldest stellar populations, we also note that such an association probably would already have been identified using the host-galaxy morphology, spectroscopy, or optical and infrared photometry (*8, 23, 37–41*).

KPNO Image Reduction and Calibration. We acquired *ugriz* imaging of SN Ia host galaxies with the T2KA and T2KB cameras mounted on the Kitt Peak National Observatory (KPNO) 2.1 m telescope in June 2009, March 2010, May 2010, October 2010, and December 2010. The raw images were processed using standard IRAF[1] reduction routines. A master bias frame was created from the median stack of the bias exposures taken each night, and subtracted from the flat field and from images of the host galaxies. For each run, we constructed a median dome-flat exposure that we used to correct the host-galaxy images. To improve the flat-field correction, a median stack of all host-galaxy frames was computed after removing all objects detected using SExtractor (*42*).

Even after dividing images by the flat field and by stacked, object-subtracted science images, the edge to the south of the T2KB CCD array showed a $> 5\%$ spatially dependent background variation. To remove this poorly corrected region of the detector, we trimmed the 400 pixel columns closest to south edge of the T2KB pixel array, after overscan subtraction. We constructed a fringe model for *z*-band images from object-subtracted science images, and scaled the model to best remove fringing from the affected images.

Lick Observatory Image Reduction and Calibration. We used the bias and flat-field corrected *BVRI* "template" images of the host galaxies of SN Ia acquired after the SN had faded, as part of the LOSS follow-up program (*43*). The imaging was obtained using the 0.76 m Katzman Automatic Imaging Telescope (KAIT) and the 1 m Anna Nickel telescope at Lick Observatory (*44*). During the period when the observations were taken, the CCD detector that was mounted on KAIT was replaced twice, while the *BVRI* filter set was replaced once.

Astrometric and Photometric Calibration of KPNO and Lick Observatory Imaging. We used the *Astrometry.net* routine (*45*), which matches sources in each input

---

[1]http://iraf.noao.edu/

image against positions in the USNO-B catalog, to generate a World Coordinate System (WCS) for each KPNO 2.1 m, KAIT, and Nickel image. After updating each image with the WCS computed by *Astrometry.net*, we performed a simultaneous astrometric fit that included every exposure of each host galaxy across all passbands using the `SCAMP` package (*46*), and the 2MASS (*47*) point-source catalog as the reference.

The resulting WCS solution was passed to `SWARP` and used to resample all images to a common pixel grid. To extract stellar magnitudes, we next used `SExtractor` (*42*) to measure magnitudes inside circular apertures with $4''$ radius. `PSFEx` (*48*) was used to fit a Moffat point-spread function (PSF) model and calculate an aperture correction for each image. We computed *ugriz* or *BVRI* zeropoints from the stellar locus using the publicly available `big macs`[2] package developed by the authors (*49*). The routine synthesizes the expected stellar locus for an instrument and detector combination using the wavelength-dependent transmission and a spectroscopic model of the SDSS stellar locus.

Host-Galaxy Photometry. To measure UV emission from host galaxies, we used both FUV and NUV imaging from the All-Sky Imaging Survey and Medium Imaging Survey performed by the *Galaxy Evolution Explorer (GALEX)* (*50*) satellite. The *GALEX* FUV passband has a central wavelength of 1528 Å and a PSF full width at half-maximum intensity (FWHM) of $\sim 6''$, while the central wavelength of the NUV passband is 2271 Å and the PSF FWHM is $\sim 4.5''$. Photometry at optical wavelengths was measured from *ugriz* images taken with the SDSS or the KPNO 2.1 m telescope, or from *BVRI* images taken with KAIT or the 1 m Nickel telescope at Lick Observatory. All optical images were convolved to have a PSF of $\sim 4.5''$ to match that of the *GALEX* NUV images before extracting host-galaxy photometry.

When assembling mosaics of host-galaxy images, we record the MJD of each image. We exclude exposures taken from between two weeks prior to through 210 days past the date when the SN reached *B*-band maximum. For the SN host galaxies that have images without contaminating flux, we resample all exposures to a common grid centered on the SN explosion coordinates using the `SWarp` (*51*) software program. We measure the host-galaxy flux within a circular $r = 5$ kpc aperture, and compute K-corrections using `kcorrect` (*52*). When both UV and optical host photometry are available, we estimate the star-formation surface density using the PEGASE2 (*53*) stellar population synthesis models. In Table S4, we list measured light-curve parameters, host-galaxy measurements, and Hubble residuals.

R_V **and the Hubble Residuals of SN in Regions with High NUV Surface Brightness.** Figure S5 plots Hubble residuals against A_V for MLCS2k2 distance moduli computed using $R_V = 1.8$ and $R_V = 3.1$.

---

[2]https://code.google.com/p/big-macs-calibrate/

FUV Surface Brightness. Figure S4 shows that the FUV surface brightness yields comparably small Hubble-residual scatter as NUV surface brightness. Among the Hubble residuals of the $N = 16$ SN Ia in environments brighter than $25.0\,\mathrm{mag\,arcsec^{-2}}$, the root-mean-square scatter is $0.082\pm0.010\,\mathrm{mag}$. When we examine only the $N = 10$ SN Ia with distance modulus statistical uncertainty $\sigma_{\mu_{\mathrm{SN}}} < 0.075$ mag, the root-mean-square scatter is $0.067\pm0.013\,\mathrm{mag}$. Additional statistics are listed in Table 1.

Color Composite Images of Explosion Environments. Figure S6 displays panels of SDSS color composite images of the host-galaxy environments for SN Ia whose circular $r = 5\,\mathrm{kpc}$ apertures have, respectively, high and low average NUV surface brightness. These images show that SN that occur within the host-galaxy outskirts, as well as in small low-mass galaxies, have low average NUV surface brightness within the aperture.

Si II Velocity. In Figure S7, we show the velocities of SN Ia that have Si II measurements within seven days of B-band maximum brightness against NUV surface brightness within the circular $r = 5\,\mathrm{kpc}$ aperture. The highly standardizable population found in high surface brightness regions shows no strong differences in the distributions of Si II velocities near maximum brightness.

References

34. A. U. Landolt, *AJ* **104**, 340–371 (1992).

35. D. J. Fixsen *et al.*, *ApJ* **473**, 576 (1996).

36. P. Nugent, A. Kim, S. Perlmutter, *PASP* **114**, 803–819 (2002).

37. R. R. Gupta *et al.*, *ApJ* **740**, 92 (2011).

38. C. B. D'Andrea *et al.*, *ApJ* **743**, 172 (2011).

39. J. Johansson *et al.*, *MNRAS* **435**, 1680–1700 (2013).

40. B. T. Hayden *et al.*, *ApJ* **764**, 191 (2013).

41. Y.-C. Pan *et al.*, *MNRAS* **438**, 1391–1416 (2014).

42. E. Bertin, S. Arnouts, *AJ* **117**, 393–404 (1996).

43. A. V. Filippenko, W. D. Li, R. R. Treffers, M. Modjaz, presented at the IAU Colloq. 183: Small Telescope Astronomy on Global Scales, ed. by B. Paczynski, W.-P. Chen, & C. Lemme, vol. 246, p. 121.

44. M. Ganeshalingam *et al.*, *ApJS* **190**, 418–448 (2010).

45. D. Lang, D. W. Hogg, K. Mierle, M. Blanton, S. Roweis, *AJ* **139**, 1782–1800 (2010).

46. E. Bertin, presented at the Astronomical Data Analysis Software and Systems XV, ed. by C. Gabriel, C. Arviset, D. Ponz, & S. Enrique, vol. 351, p. 112.

47. M. F. Skrutskie *et al.*, *AJ* **131**, 1163–1183 (2006).

48. E. Bertin, presented at the Astronomical Data Analysis Software and Systems XX, ed. by I. N. Evans, A. Accomazzi, D. J. Mink, A. H. Rots, vol. 442, p. 435.

49. P. L. Kelly *et al.*, *MNRAS* **439**, 28–47 (2014).

50. D. C. Martin *et al.*, *ApJ* **619**, L1–L6 (2005).

51. E. Bertin *et al.*, presented at the Astronomical Data Analysis Software and Systems XI, ed. by D. A. Bohlender, D. Durand, & T. H. Handley (San Francisco: ASP), p. 228.

52. M. R. Blanton, S. Roweis, *AJ* **133**, 734–754 (2007).

53. M. Fioc, B. Rocca-Volmerange, *ArXiv e-prints* (1999).

Light-Curve Dataset	Filters	References
Lick Observatory Supernova Search (LOSS)	*BVRI*	*(55)*
CfA2	*(U)BVRI*	*(56)*
CfA3	*(U)BVRIr'i'*	*(57)*
CfA4	*(U)BVr'i'*	*(58)*
Carnegie Supernova Project (CSP)	*(u)BVgri*	*(59, 60)*

Table S1: SN Ia light-curve samples used for the analysis. When fitting SN light curves, we did not include measured *U*- or *u*-band magnitudes.
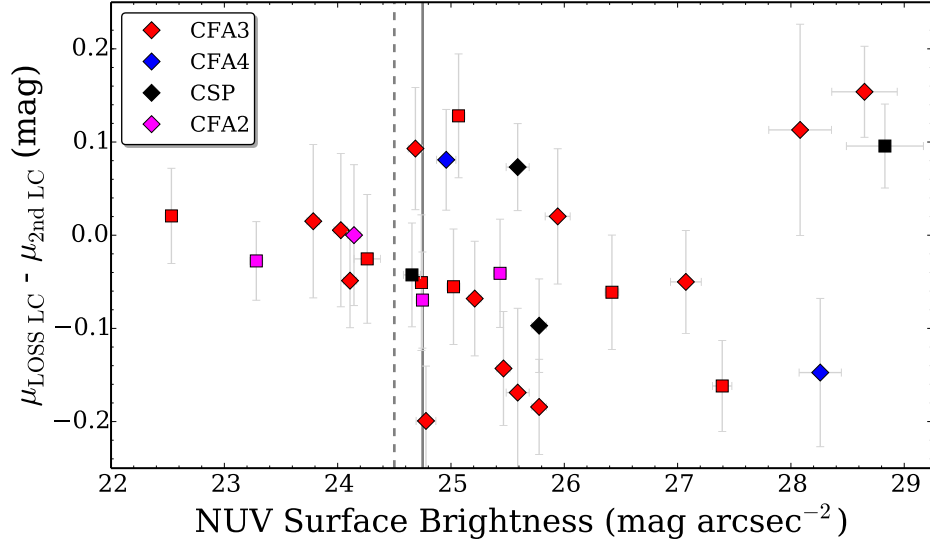
Fig. S1: Difference between MLCS2k2 distance moduli μ measured using LOSS and a second published light curve against NUV surface brightness inside a circular aperture with 5 kpc radius. SN that erupt in regions with a high near-UV surface brightness may show greater agreement between distance measurements from independent light curves. Diamonds mark SN having $z > 0.02$ (included in the Hubble-residual sample), while squares mark SN having $z < 0.02$. The parallel vertical lines show the $24.5 \, \mathrm{mag \, arcsec^{-2}}$ (dashed) and $24.75 \, \mathrm{mag \, arcsec^{-2}}$ (solid) NUV surface brightness upper limits used to construct samples of SN Ia having low Hubble residual scatter.

Criterion	SN
$N_{\mathrm{DOF}} > 5$	307
$\chi^2_\nu < 2$	292
$z > 0.02$	165
$A_V < 0.4\,\mathrm{mag}$	143
$-0.35 < \Delta < 0.4$	107
MLCS2k2	107
Not SNF20080522-000	106
MW $A_V < 0.5\,\mathrm{mag}$	103
Uncontaminated FUV; NUV	83
$R_V = 1.8$ Hubble residual $< 0.3\,\mathrm{mag}$	77
Uncontaminated FUV; NUV; *ugriz* or *BVRI*	67
$R_V = 1.8$ Hubble residual $< 0.3\,\mathrm{mag}$	61

Table S2: Construction of SN sample. χ^2_ν is the reduced chi-squared statistic calculated for the MLCS2k2 ($R_V = 1.8$) light-curve fits. A_V is the best-fitting extinction value computed by MLCS2k2. Milky Way extinction is computed from foreground dust maps (*54*). We exclude host-galaxy images taken from 14 days prior to through 210 days after B-band maximum light.
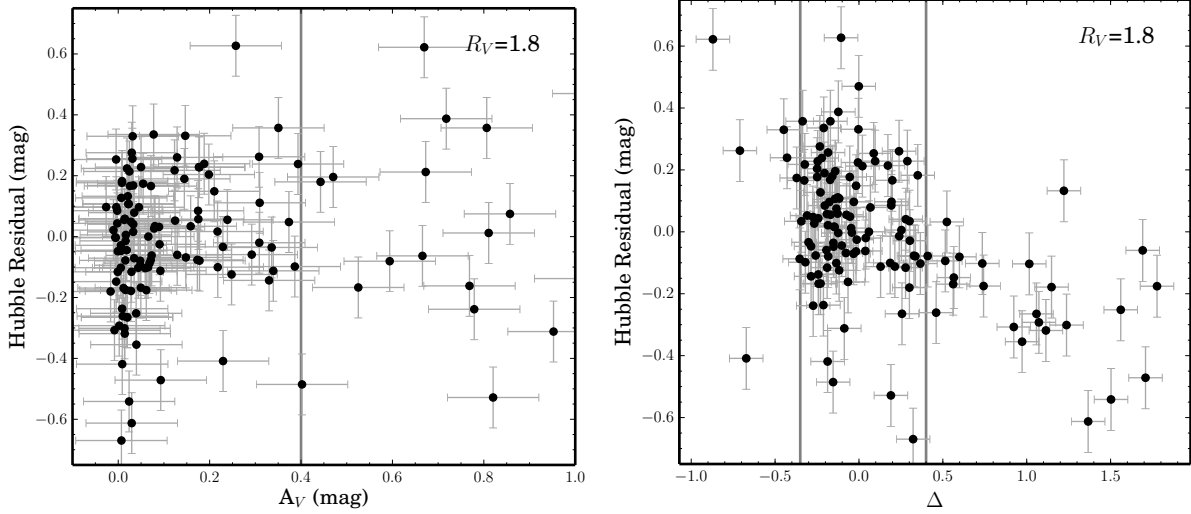

Fig. S2: Hubble residuals plotted against MLCS2k2 $R_V = 1.8$ light-curve parameters. When constructing our sample of SN Ia light curves, we apply the $A_V < 0.4$ upper limit shown in the left panel by the vertical line. We include only SN with decline-rate parameter $-0.35 < \Delta < 0.7$ marked by the pair of vertical lines in the right panel.
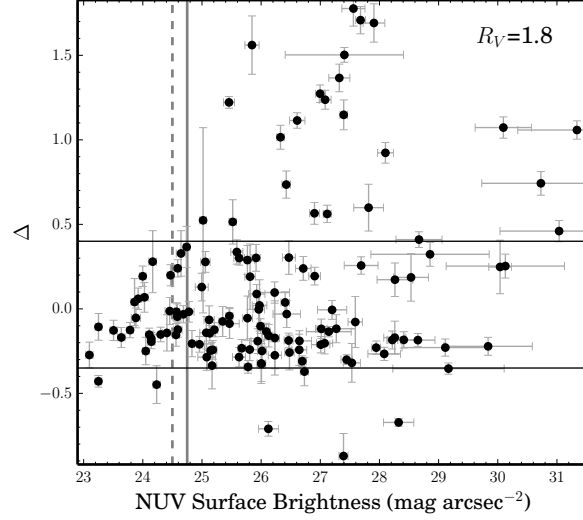
Fig. S3: MLCS2k2 light-curve decline parameter Δ against NUV surface brightness inside circular apertures with 5 kpc radius centered on the SN. More rapidly declining SN Ia have greater values of Δ and are, on average, less luminous explosions. The parallel horizontal lines are the $-0.35 < \Delta < 0.7$ limits that we apply to construct our light-curve sample, while the parallel vertical lines show the $24.5 \, \mathrm{mag\,arcsec^{-2}}$ (dashed) and $24.75 \, \mathrm{mag\,arcsec^{-2}}$ (solid) NUV surface brightness upper limits.
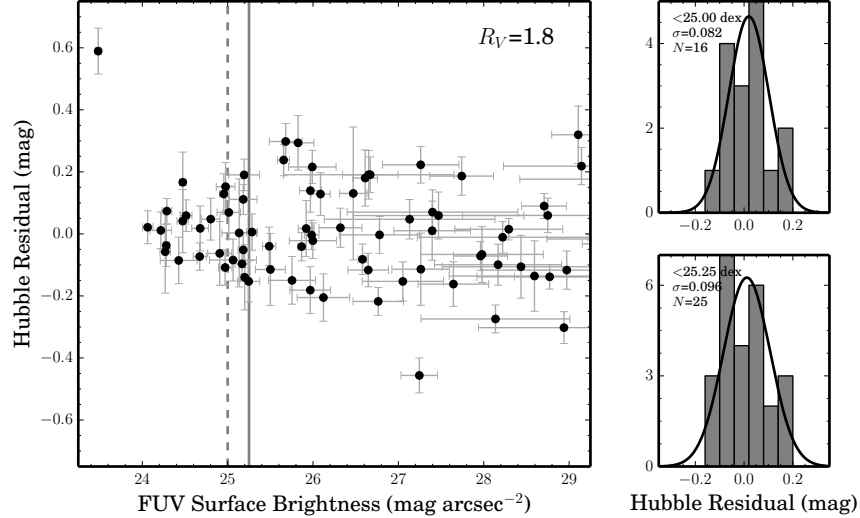
Fig. S4: SN Ia in regions with high NUV (upper) and FUV (lower) surface brightness ($<24.75 \, \mathrm{mag\,arcsec^{-2}}$ and $25.25 \, \mathrm{mag\,arcsec^{-2}}$, respectively) inside a circular aperture with 5 kpc radius exhibit smaller Hubble-residual dispersion.

17
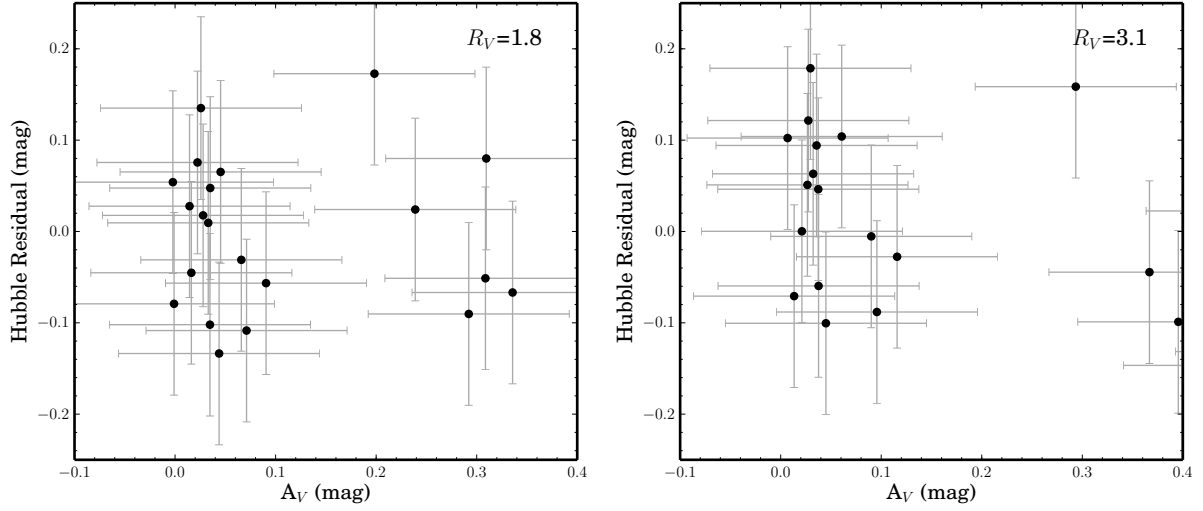
Fig. S5: Hubble residuals against MLCS2k2 A_V parameter for $R_V = 1.8$ and $R_V = 3.1$ model dust extinction laws for SN with NUV surface brightness $<24.75\,\mathrm{mag\,arcsec^{-2}}$ inside a circular $r = 5\,\mathrm{kpc}$ aperture centered at the SN position. As shown in Table 1, distance moduli computed using MLCS2k2 with an $R_V = 1.8$ dust extinction law exhibit a smaller dispersion among their Hubble residuals, than when computed using an $R_V = 3.1$ model dust extinction law.
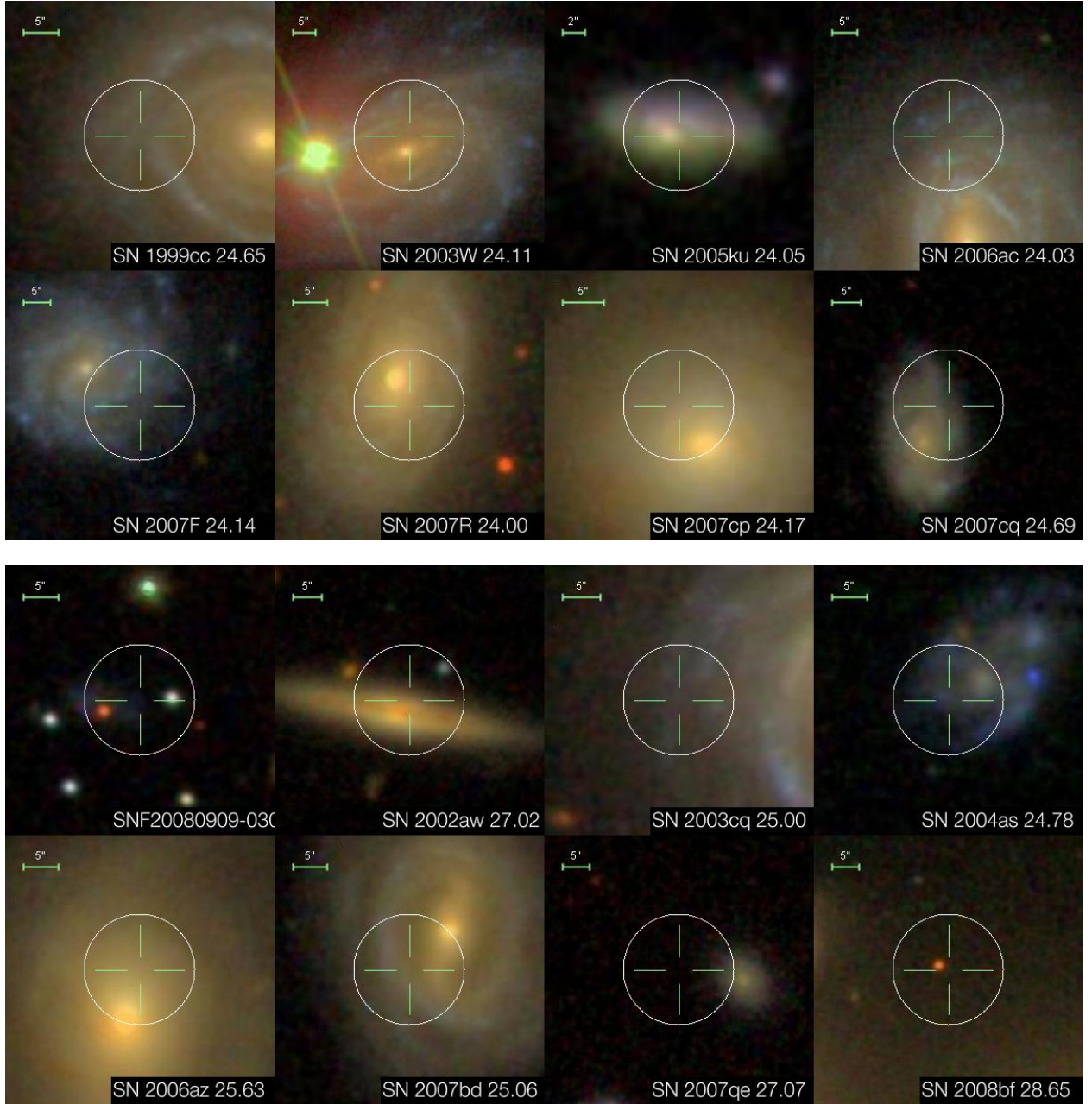
Fig. S6: Representative samples of explosion sites of SN Ia with high and low *GALEX* NUV surface brightness within a 5 kpc radius of the SN coordinates. White circles represent the apertures used for photometry. The upper mosaic shows SDSS color composite images of the host galaxies where the aperture NUV surface brightnesses is brighter than $24.75 \, \mathrm{mag \, arcsec^{-2}}$, while the lower panels contain images of SN with environments that have lower NUV surface brightness. Text below each galaxy describes the NUV surface brightness, while the crosshairs are centered on the location of the explosion.

19
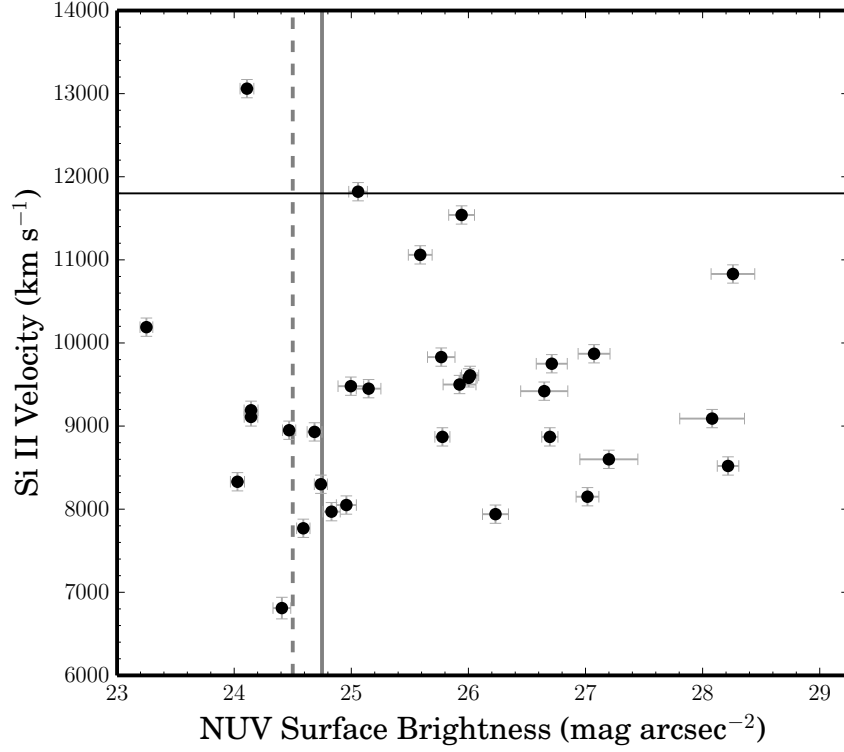
Fig. S7: NUV surface brightness against Si II photospheric velocity of SN Ia. Horizontal line shows the $11{,}800\,\mathrm{km\,s^{-1}}$ line used by Wang et al. (2009) to separate low- and high-velocity SN Ia (*9*). The population erupting in apertures with high NUV surface brightness does not differ strongly from those found in lower surface brightness regions.

Table S3: Host-Galaxy Environment

| Name	z_{helio}	NUV SB	FUV SB	SFR Density dex	HR $R_V = 1.8$	HR $R_V = 3.1$
SN 1997dg	0.034	F	F	L	0.30±0.09	0.06±0.11
SN 1999cc	0.031	B	F	H	-0.11±0.12	-0.09±0.12
SN 1999dg	0.022	F	F	L	-0.06±0.09	-0.01±0.09
SN 2000dn	0.032	F	F	L	0.19±0.06	0.24±0.06
SN 2000fa	0.021	B	B	H	-0.09±0.05	-0.15±0.06
SN 2001br	0.021	F	F	L	0.23±0.06	0.22±0.07
SN 2001cj	0.024	F	F	L	0.10±0.04	0.14±0.04
SN 2001ck	0.035	B	B	H	0.02±0.06	0.06±0.06
SN 2001cp	0.022	F	F	L	-0.00±0.05	0.02±0.06
SN 2001ie	0.031	F	F	L	-0.13±0.12	-0.18±0.15
SN 2002aw	0.026	F	F	⋯	-0.16±0.07	-0.23±0.09
SN 2002de	0.028	B	B	⋯	0.08±0.04	0.02±0.05
SN 2002eb	0.028	F	F	L	0.02±0.03	0.01±0.04
SN 2002el	0.030	F	F	L	-0.30±0.05	-0.25±0.05
SN 2002hu	0.037	F	F	L	-0.15±0.06	-0.10±0.07
SN 2003U	0.028	B	B	L	-0.13±0.10	-0.10±0.10
SN 2003W	0.020	B	B	H	-0.07±0.04	-0.13±0.05
SN 2003ch	0.025	F	F	L	0.18±0.09	0.23±0.09
SN 2003cq	0.033	F	F	H	-0.14±0.08	-0.21±0.09
SN 2003gn	0.035	F	F	L	0.20±0.06	0.16±0.06
SN 2003kc	0.033	B	B	⋯	-0.05±0.13	-0.10±0.20
SN 2004as	0.031	F	B	H	0.12±0.05	0.07±0.05
SN 2004at	0.022	F	F	L	-0.08±0.05	-0.03±0.05
SN 2004bg	0.021	F	F	L	-0.03±0.05	0.01±0.05
SN 2004br	0.023	F	F	L	-0.27±0.04	-0.22±0.05
SN 2004bw	0.021	B	B	H	-0.05±0.06	0.00±0.06
SN 2004ef	0.031	F	F	⋯	-0.11±0.05	-0.14±0.05
SN 2004gu	0.045	F	F	L	-0.06±0.05	-0.14±0.06
SN 2005ag	0.079	F	F	L	-0.13±0.04	-0.16±0.05
SN 2005bg	0.023	B	B	⋯	0.03±0.05	0.05±0.06
SN 2005eq	0.030	F	F	L	0.00±0.05	-0.02±0.06
SN 2005eu	0.035	F	F	L	-0.03±0.06	0.02±0.06
SN 2005hc	0.046	F	F	L	0.24±0.05	0.29±0.06
SN 2005iq	0.034	F	F	⋯	0.22±0.05	0.27±0.05
SN 2005ku	0.050	B	B	H	0.17±0.10	0.16±0.13
SN 2005ms	0.025	F	F	L	0.22±0.06	0.27±0.07
SN 2006S	0.032	F	B	L	0.20±0.05	0.17±0.07
SN 2006ac	0.023	B	B	H	0.05±0.10	0.09±0.11
SN 2006an	0.064	F	F	L	0.08±0.07	0.12±0.07
SN 2006az	0.031	F	F	L	-0.21±0.05	-0.16±0.05
SN 2006cf	0.042	B	B	H	0.08±0.09	0.12±0.09
SN 2006cj	0.068	F	F	L	0.15±0.07	0.19±0.07
SN 2006cp	0.022	F	F	L	0.03±0.06	0.01±0.07
SN 2006cq	0.048	F	F	L	0.19±0.09	0.19±0.11
SN 2006en	0.032	B	B	⋯	0.02±0.07	-0.04±0.09
SN 2006et	0.022	F	F	⋯	0.02±0.10	-0.07±0.12
SN 2006lu	0.053	B	B	⋯	-0.08±0.07	-0.07±0.08
SN 2006mp	0.023	F	B	⋯	0.16±0.08	0.14±0.10
SN 2006oa	0.060	F	F	L	0.13±0.07	0.16±0.07
SN 2006on	0.070	F	F	L	-0.13±0.11	-0.23±0.15
SN 2006py	0.060	F	F	L	-0.10±0.10	-0.20±0.11
SN 2006sr	0.024	B	B	H	0.14±0.07	0.18±0.07
SN 2007F	0.024	B	B	H	0.07±0.05	0.10±0.06
SN 2007R	0.031	B	B	H	0.05±0.07	0.10±0.07
SN 2007ae	0.064	F	F	⋯	-0.20±0.08	-0.15±0.08

Name	z_{helio}	NUV SB	FUV SB	SFR Density dex	HR $R_V = 1.8$	HR $R_V = 3.1$
SN 2007bd	0.030	F	B	H	-0.15±0.07	-0.10±0.07
SN 2007bz	0.022	B	B	H	0.60±0.07	0.54±0.10
SN 2007cp	0.037	B	B	H	0.01±0.17	0.05±0.18
SN 2007cq	0.026	B	B	H	-0.10±0.06	-0.06±0.06
SN 2007is	0.030	B	B	H	-0.06±0.10	-0.03±0.13
SN 2007jg	0.040	F	F	L	0.20±0.08	0.24±0.09
SN 2007qe	0.024	F	F	$\cdots$	0.05±0.06	0.03±0.07
SN 2008Q	0.008	F	F	L	-4.75±0.10	-4.73±0.08
SN 2008Z	0.021	F	F	L	0.33±0.09	0.25±0.11
SN 2008ar	0.026	F	F	L	0.30±0.06	0.33±0.07
SN 2008bf	0.024	F	F	L	-0.01±0.05	0.04±0.05
SN 2008bz	0.060	F	F	L	0.07±0.08	0.11±0.08
SN 2008cf	0.046	F	B	$\cdots$	-0.08±0.07	-0.03±0.07
SN 2008dr	0.041	F	F	$\cdots$	0.00±0.06	0.02±0.07
SN 2008fr	0.039	F	F	L	-0.45±0.06	-0.40±0.06
SN 2008gl	0.034	F	F	$\cdots$	-0.03±0.08	0.02±0.08
SN 2008hj	0.038	F	F	L	0.02±0.09	0.07±0.09
SN 2009D	0.025	F	F	L	-0.11±0.06	-0.07±0.07
SN 2009ad	0.028	F	F	L	-0.02±0.06	0.03±0.06
SN 2009al	0.022	F	F	L	0.21±0.06	0.08±0.07
SN 2009do	0.040	F	F	L	-0.09±0.07	-0.07±0.08
SN 2009lf	0.046	F	F	L	-0.70±0.07	-0.65±0.07
SN 2009na	0.021	B	B	H	-0.03±0.07	-0.01±0.08
SN 2010ag	0.034	F	F	$\cdots$	-0.18±0.08	-0.25±0.10
SN 2010dt	0.053	F	F	L	0.14±0.21	0.18±0.22
SNF20080514-002	0.022	F	F	L	0.07±0.06	0.12±0.06
SNF20080522-011	0.038	F	F	L	0.01±0.06	0.06±0.06
SNF20080909-030	0.031	F	F	L	-0.11±0.12	-0.14±0.13

Table S4: The NUV and FUV surface brightnesses are measured within a circular $r = 5\,\text{kpc}$ aperture centered at the SN position. "NUV" and "FUV" columns show whether surface brightness measured inside the aperture is brighter (B) or fainter (F) than the 24.75 and 25.25 mag arcsec^{-2} thresholds, respectively. Similarly, the "SFR Density" indicates whether the star-formation density is lower (L) or higher (H) than the -2.25 dex threshold. The "HR" columns show the Hubble residuals of each SN Ia from the best-fitting redshift-distance relation for $R_V = 1.8$ and $R_V = 3.1$ MLCS2k2 light-curve fits.